Multi-Scale Continuum Modeling of Mediated Electron Transfer in 3D Living Bio-Anodes

Author Information

Tali Dotan,[1] Leyna H. Nguyen,[1], Christian Ogata,[1] Eleanor R. Murphy,[1] Ariel L. Furst[1*]

1 Department of Chemical Engineering, Massachusetts Institute of Technology, Cambridge, MA, USA

*Correspondence to: Ariel L. Furst (afurst@mit.edu)

Abstract

Bioelectrochemical systems, in which electroactive microbes transfer electrons across biological-abiotic interfaces, represent a vital technology for sustainable energy production, chemical synthesis, and environmental remediation. However, these systems are constrained by a two-dimensional design paradigm, with reactors achieving power densities 10–100-times lower than theoretical limits because conventional architectures restrict electron transfer to a single layer at the electrode surface. Here, we establish quantitative design rules that govern three-dimensional bio-electrochemical function driven by small-molecule electron transfer mediators. Through integrated theory, simulation, and engineered biofilm validation, we identify two distinct scale-dependent transport regimes: a macroscopic regime where bulk mediator availability governs active layer expansion and a microscopic regime where microbial packing geometry controls local redox cycling, both of which are fundamentally constrained by mass transport. We validate these scaling laws experimentally using agarose-encapsulated *Shewanella oneidensis* MR-1 and demonstrate that rational mediator loading and cellular packing can elevate current densities beyond 0.5 A m^{-2}, exceeding two-dimensional performance ceilings. These design principles provide a generalizable blueprint for engineering high-performance biocatalytic systems and offer researchers studying natural biofilms a mechanistic framework to decode internal transport architecture.

Introduction

Electroactive microbes (EAMs), microbes capable of generating electrical current through transfer of electrons directly to an anode, have the potential to revolutionize sustainable energy generation, chemical synthesis, and environmental remediation through incorporation into bio-electrochemical systems. However, reactors that harness EAMs operate at macroscopic current densities (1-5 A m^{-2}) much lower than the mass-transport-limited theoretical maximum for dense microbial catalysts. This performance gap is not due to fundamental limitations in microbial extracellular electron transfer (EET), which can achieve electron flux rates exceeding 10 A m^{-2} at optimized interfaces, but instead from a persistent architectural constraint: conventional designs restrict active biomass to surface-confined monolayers. Historically, engineering of these technologies has focused on direct electron transfer (DET), relying on outer-membrane cytochromes or conductive appendages to directly contact solid electrodes. Specifically, in electroactive species such as *Geobacter* spp., direct transport is facilitated by a matrix of conductive pili capable of sustaining efficient charge transfer across distances up to 80 μm[1,2]. Conversely, in non-conductive biofilms such as *Shewanella* spp., DET is restricted to distances of only a few nanometers[3,4], inherently confining charge translocation to a two-dimensional surface monolayer.

Once a single cellular monolayer saturates the electrode interface, the geometric ceiling is absolute: additional accumulated biomass becomes electronically insulated from the external circuit (**Figure 1a**). To circumvent this limitation, the vast majority of literature continues to optimize bio-electrochemical systems by maximizing electroactive surface area[5–9]. This approach maintains a two-dimensional paradigm that is fundamentally incapable of achieving the volumetric power densities required for commercial scaling.

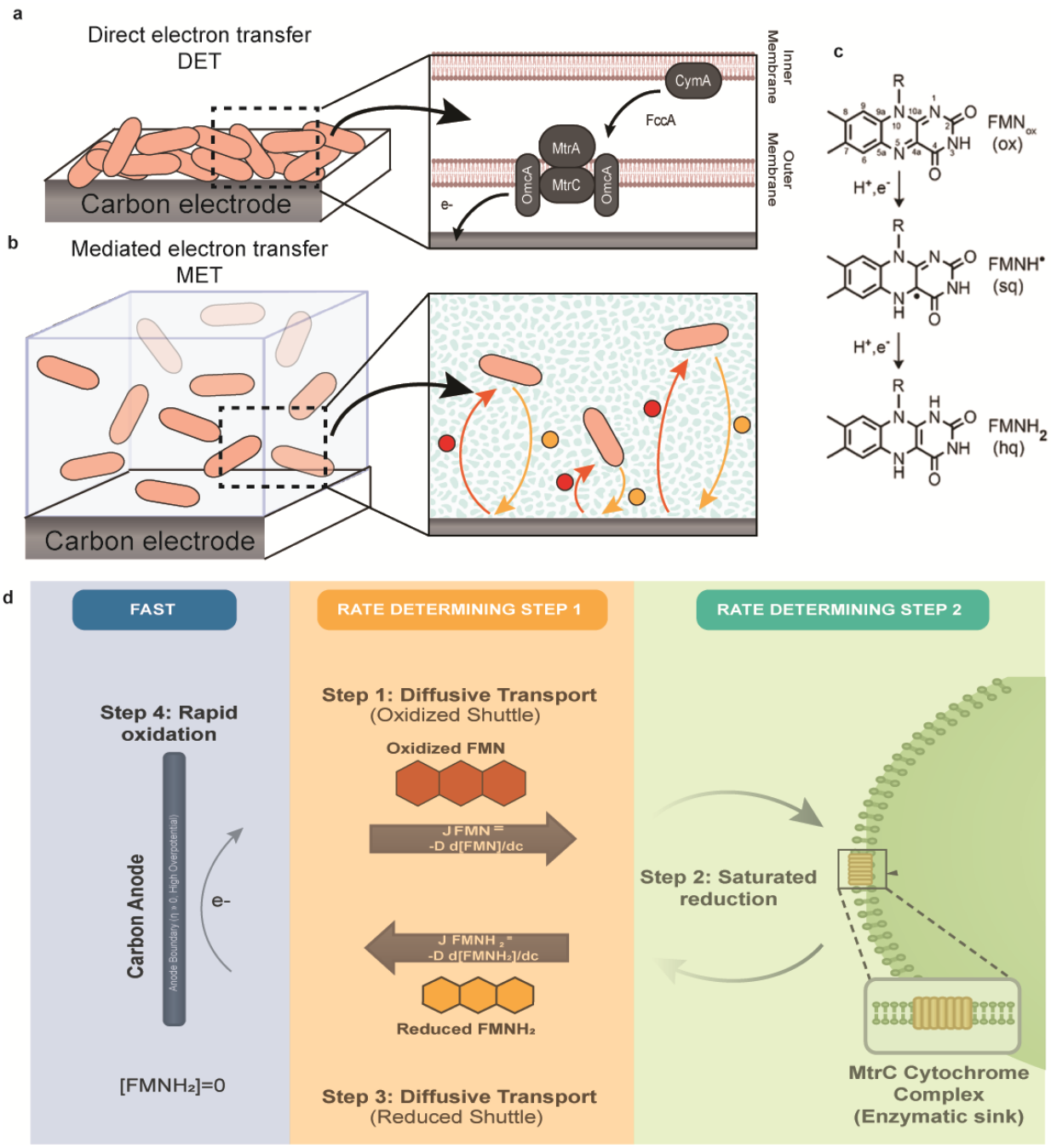
The path forward lies not in incrementally optimizing interfaces by boosting surface area, but in reimagining bio-electrodes as three-dimensional catalytic volumes. Model electroactive organisms such

as *Shewanella oneidensis* MR-1 possess a dual respiratory capability that enables this transition: while they perform DET through surface cytochromes, they simultaneously secrete soluble electron transfer mediators, specifically flavin mononucleotide (FMN) and riboflavin[10,11]. Through such mediated electron transfer (MET), electron transfer is decoupled from direct physical contact between the microbe and electrode. Mediators can transfer electrons across distances spanning tens to hundreds of microns, allowing cells distributed throughout thick biofilms or synthetic hydrogel matrices to contribute to the total current density[4,10,12] (**Figure 1b**).

Yet the promise of volumetric current density remains largely unrealized in practice because shifting from two-dimensional surfaces to three-dimensional volumes introduces an acute transport-reaction trade-off[13]. While MET unlocks volumetric cell recruitment, this recruitment is stringently bounded by the diffusive supply of redox mediators competing against rapid cellular consumption. As a biofilm or bio-hybrid matrix thickens, interior cells face severe mediator depletion that leaves most of the architecture functionally dormant[14,15].

Here, we address this challenge directly by establishing predictive physical principles that map these internal transport limits. Through combined analytical theory, multiscale computational modeling, and empirical validation using engineered *S. oneidensis*-laden hydrogels, we uncover two fundamental power-law scaling regimes. These design rules operate universally across both native biofilms and synthetic living materials, providing a quantitative roadmap to rationally engineer high-performance three-dimensional bioelectrodes.

Figure 1. Mechanisms and kinetic sequence of mediated electron transfer in 3D bio-anodes.



a. Direct electron transfer (DET) mechanism showing monolayer cell attachment to a flat carbon electrode, controlled by outer-membrane cytochromes (CymA, FccA, MtrA, MtrC, OmcA). b. Mediated electron transfer (MET) mechanism within a 3D hydrogel matrix, utilizing mobile flavin shuttles to transport electrons to the anode collector. c. Chemical structures and two-electron, two-proton reduction pathway of flavin mononucleotide from oxidized (FMN_{ox}) through semiquinone ($FMNH^{\cdot}$) to fully reduced hydroquinone ($FMNH_2$) forms. d. Schematic of the four-step MET kinetic cycle, including rate-determining diffusive transport (Steps 1 and 3) and zero-order enzymatic reduction at saturated MtrC cytochromes (Step 2) relative to rapid anodic oxidation (Step 4).

Results

Theory

The modeling of high-performance three-dimensional bio-anodes requires a quantitative understanding of the interplay between mass transport and metabolic kinetics. To characterize the performance of *S. oneidensis* MR-1 encapsulated within a hydrogel matrix, we established an enzymatic reaction-diffusion framework focusing on the behavior of Flavin Mononucleotide (FMN) as the primary MET shuttle.

Direct versus Mediated Electron Transfer in S. oneidensis

The physiological prevalence of MET over DET pathways in *S. oneidensis* biofilms is well-supported by quantitative genetic and electrochemical analyses. Landmark investigations demonstrate that, when mediators such as riboflavin are washed away from active biofilms, current density decreases by over 70%, proving that secreted flavins are indispensable for efficient EET[10]. Further, studies of genetic knockouts targeting flavin secretion machinery, such as the bacterial flavin adenine dinucleotide exporter (*Δbfe*), confirm that these shuttles account for roughly 75% of total EET capacity to insoluble substrates[3]. Although flavins can transiently bind to membrane-associated cytochromes and expedite local interfacial charge transfer[11], sustained electronic connectivity across multi-cellular length scales is dependent on the extracellular diffusion of these molecules in their unbound form[16].

Chemically, MET is driven by the sequential two-electron, two-proton ($2e^-/2H^+$) proton-coupled electron transfer (PCET) pathway of Flavin Mononucleotide[3,17] (**Figure 1c**). Within the biofilm or hydrogel volume, FMN dynamically transitions across three distinct oxidation states: starting in its fully oxidized quinone form (FMN_{ox}), accepting a single electron and proton to form a transient neutral semiquinone radical intermediate ($FMNH\cdot$), and completing a second reduction step to yield the fully reduced hydroquinone species ($FMNH_2$)[11] (**Figure 1c**). Soluble FMN_{ox} diffuses to the cell surface where outer-

membrane cytochromes reduce it to $FMNH_2$[17,18], which then diffuses back to the electrode interface for rapid electrochemical re-oxidation back to FMN_{ox}[10] (**Figure 1c,d**). This continuous molecular cycling establishes the closed redox loop necessary to sustain volumetric charge translocation across the matrix[19].

Flavin Concentration Framework

Under steady-state conditions, the concentration profile of the oxidized electron shuttle within the hydrogel is governed by the balance between diffusive flux and metabolic consumption[20–22]. To model this mediated charge transport, we conceptualize the closed redox loop as a four-step reaction-diffusion pathway (**Figure 1d**):

Step 1: Diffusive transport of oxidized flavin (FMN_{ox}) from the matrix toward the bacterial cell surface.

Step 2: Saturated enzymatic reduction of FMN_{ox} to $FMNH_2$ at outer-membrane cytochrome complexes (e.g., MtrC), operating as a zero-order catalytic sink (Rate-Determining Step 2).

Step 3: Diffusive transport of reduced flavin ($FMNH_2$) back through the gel matrix toward the electrode (Rate-Determining Step 1).

Step 4: Rapid electrochemical re-oxidation of $FMNH_2$ at the carbon anode interface.

The anode overpotential is maintained high ($\eta \gg 0$), therefore, interfacial oxidation (Step 4) is electrochemically fast, maintaining $[FMNH_2]_{x=0} \approx 0$ at the electrode surface. Consequently, total charge translocation is governed entirely by the competition between matrix diffusion (Steps 1 & 3) and enzymatic cell-surface kinetics (Step 2) (**Figure 1d**).

Assuming a planar electrode geometry with a large aspect ratio relative to hydrogel thickness, lateral concentration gradients are negligible. We therefore reduce the system to a one-dimensional spatial

domain along the x-axis, defined as the normal distance extending from the electrode interface (x = 0) into the hydrogel matrix (x > 0).

Under steady-state conditions ($\frac{\partial C}{\partial t} = 0$), transient accumulation terms vanish, and mass conservation within the bio-anode hydrogel is governed by a one-dimensional steady-state reaction-diffusion equation. To derive the spatial concentration profile across the film, the mass balance for the reduced mediator (C_{red}) along the axis x perpendicular to the electrode surface is expressed as:

$$D \cdot \frac{\partial^2 C_{Red}}{\partial x^2} = -D \cdot \frac{\partial^2 C_{Ox}}{\partial x^2} = -R_c \quad (1)$$

where D is the effective diffusion coefficient in the hydrogel and R_c is the reaction term.

In the Michaelis-Menten expression:

$$R_c = \frac{\nu_{bio} \cdot C_{Ox}}{K_m + C_{Ox}} = k \quad (2)$$

where ν_{bio} (mol · m^{-3} · s^{-1}) represents the intrinsic maximum catalytic turnover rate of S. oneidensis surface enzymes, and K_m (μM) is the Michaelis constant governing the affinity between outer-membrane cytochromes and FMN_{ox}.

The Michaelis Menten coefficient has been previously studied and reported to be in the range of 0.5 to 10 μM[23,24]. Because the added exogenous flavins (100–20,000 μM) are orders of magnitude larger than naturally secreted flavins (0.25–1 μM) [10,16,25], the total mediator pool is overwhelmingly dominated by the exogenous addition, ensuring that the local concentration of oxidized mediator significantly exceeds the Michaelis–Menten constant (K_m) at the cellular surface. An intuitive perspective of this kinetic regime can be understood by examining the operational state of the bacterial

catalytic machinery. When the concentration of flavins (C_{Ox}) in the surrounding environment is exceptionally high, the specific electron-transfer enzymes and outer-membrane cytochromes on the cell surfaces become entirely saturated with the mediator[26].

Because every available active site is constantly occupied and working at maximum velocity (v_{bio}), the overall rate of metabolic electron transfer becomes entirely bottlenecked by the internal biological processing speed of the bacteria, rather than the availability of the shuttle[23,26]. Consequently, the reaction rate becomes completely decoupled from, and independent of, the redox mediator's concentration in the local environment. This state of molecular crowding at the cellular interface is what mathematically collapses the concentration-dependent Michaelis-Menten pathway into a constant, concentration-independent zero-order kinetic rate[21,27].

While this zero-order regime establishes a constant volumetric generation rate (k) for reduced flavin (FMN_{red}), the macroscopic steady-state current is ultimately governed by the physical transport of FMN_{red} to the electrode surface. Within the dense extracellular polymeric matrix, shuttle transport is constrained by steric hindrance, increased tortuosity, and non-specific matrix interactions. We hypothesize that this physical diffusion of FMN_{red} is significantly slower than its rapid enzymatic generation, operating within a transport-limited reaction–diffusion regime.

Under this transport-limited assumption, the steady-state spatial mass balance for FMN_{red} (C_{red}) along the axis x perpendicular to the electrode surface is expressed as:

$$\frac{d^2C_{Red}}{dx^2} = -\frac{k}{D} \tag{3}$$

double integration yields the spatial concentration profile:

$$C_{\mathrm{red}}(x) = \frac{k}{D}\left(\delta x - \frac{x^2}{2}\right) \tag{4}$$

To derive the concentration profile, we defined boundary conditions at the electrode-hydrogel interface $x = 0$, assuming instantaneous electrochemical conversion ($C_{\mathrm{red}}(0) = 0$). Furthermore, we enforced a vanishing concentration gradient ($\frac{\mathrm{d}C_{\mathrm{red}}}{\mathrm{d}x}\Big|_{x=\delta} = 0$), at the boundary of the active diffusion-reaction layer, δ. Applying these boundary conditions yields:

$$\delta = \sqrt{\frac{2D}{k} \cdot C_{bulk}} \tag{5}$$

To connect this concentration profile to the total steady-state current (I_{ss}) under this diffusion-limited regime ($\delta \leq L_{\mathrm{biofilm}}$) [20,27], we integrate the constant reaction rate (k) across the active layer thickness (δ) [21,28]:

$$I_{SS} = nFAk\delta = nFA\sqrt{2Dk \cdot C_{bulk}} \tag{6}$$

$$I_{SS} \propto \sqrt{C_{bulk}} \tag{7}$$

This expression demonstrates a square-root dependence on the bulk shuttle concentration, confirming that the observed scaling supports a model that is transport limited.

Dimensionless Scaling and Regime Transitions

At the electrode interface ($x = 0$), electron transfer kinetics are governed by the interfacial Damköhler number (Da_{el}), which compares the rate of interfacial charge transfer to diffusive transport across the active boundary layer. Under the applied operating overpotential ($\eta \approx 0.3$ V), $Da_{\mathrm{el}} \sim 10^6 \gg 1$, indicating that charge-transfer kinetics are several orders of magnitude faster than mediator diffusion. Consequently, the interfacial reaction is purely mass-transport limited ($c_{\mathrm{red}}(0) \approx 0$), rendering the overall steady-state current density independent of the specific interfacial exchange kinetic parameters.

To generalize this reaction-diffusion steady-state and establish the physical boundaries of this transport-limited regime, we can cast the governing system into a dimensionless form[29,30]. By normalizing the spatial coordinate against the total physical hydrogel half-thickness L, the competition between metabolic turnover and shuttle transport is governed by the zero-order Thiele Modulus Φ_0[4,13,20]:

$$\Phi_0 = L \cdot \sqrt{\frac{k}{D_{eff} \cdot C_{Ox,bulk}}} \tag{8}$$

This dimensionless parameter dictates the internal effectiveness of the 3D bio-anode. Mathematically, the critical threshold for complete mediator penetration occurs at $\Phi = \sqrt{2}$[13], corresponding to the exact condition where the active layer thickness equals the total film thickness ($\delta = L$) under zero-order reaction kinetics[27].

When $\Phi < \sqrt{2}$, the system is kinetically controlled- diffusion outpaces consumption, allowing FMN_{Ox} to uniformly penetrate the entire hydrogel matrix. Conversely, when $\Phi > \sqrt{2}$, metabolic consumption dominates. The incoming shuttle is depleted before penetrating the full hydrogel, restricting active transport to a localized layer near the interface ($\delta < L$, derived in Section 2.1) and inducing a state of metabolic inactivity within the hydrogel core.

Cell Concentration Framework

Whereas the macroscopic Thiele framework defines the global active layer thickness (δ), the local current generated within this zone is dictated by the micro-scale diffusion distance (δ_{elec}) between the encapsulated bacteria and the electrode surface. To model this local transport using an order-of-magnitude scaling analysis, we begin with the generalized steady-state 1D flux (J) across a characteristic diffusion distance L separating the cell sources from the planar electrode sink:

$$J = D_{\text{eff}} \frac{\Delta C}{d_{\text{elec}}} \tag{9}$$

Combining Fick's First Law with Faraday's Law of Electrolysis ($I = n_e FAJ$), the flux-limited current (I) collected at the electrode is expressed as:

$$I = \frac{n_e F A D_{\text{eff}} \Delta C}{d_{\text{elec}}} \tag{10}$$

where n_e is the number of transferred electrons per mediator molecule, F is Faraday's constant, A is the active electrode surface area, D_{eff} is the effective diffusion coefficient within the matrix, and ΔC is the

concentration gradient driving shuttle transport. This relationship establishes that the local current is inversely proportional to the characteristic transport distance ($I \propto 1/d_{\text{elec}}$).

In our 3D bio-anode, this critical length scale d_{elec} corresponds to the average spatial separation between the 2D planar electrode interface and the nearest active cells in the adjacent hydrogel layer. Because the bacteria are volumetrically distributed in three-dimensional space (C_{cells}), this average interfacial diffusion distance scales with 3D spatial cell packing:

$$d \approx (V_{cell})^{1/3} \propto \left(\frac{1}{C_{cells}}\right)^{1/3} \tag{11}$$

$$d \propto C_{\text{cells}}^{-1/3} \tag{12}$$

Substituting this geometric dependence back into our flux-limited current expression yields the cubic-root scaling law:

$$I = \frac{n_e F A D_{\text{eff}} \Delta C}{C_{\text{cells}}^{-1/3}} \quad \Longrightarrow \quad I \propto C_{\text{cells}}^{1/3} \tag{13}$$

This demonstrates that under micro-scale diffusion-limited interfacial transport, total current scales directly with the $1/3$ power of cellular loading ($C_{\text{cells}}^{1/3}$). This micro-scale derivation complements our macroscopic Thiele modulus analysis, providing the dual-scale theoretical foundation used to ground our discrete-particle COMSOL models and validate our experimental trends.

Finally, the oxidation of reduced flavins at the electrode surface releases protons ($FMNH_2 \rightarrow FMN + 2H^+ + 2e^-$), which could theoretically generate local pH micro-gradients near the interface. Significant local acidification can alter the formal redox potential of the shuttle (via a Nernstian shift of ~ 59 mV/pH unit) or decrease biological reaction rates. However, because proton diffusion in

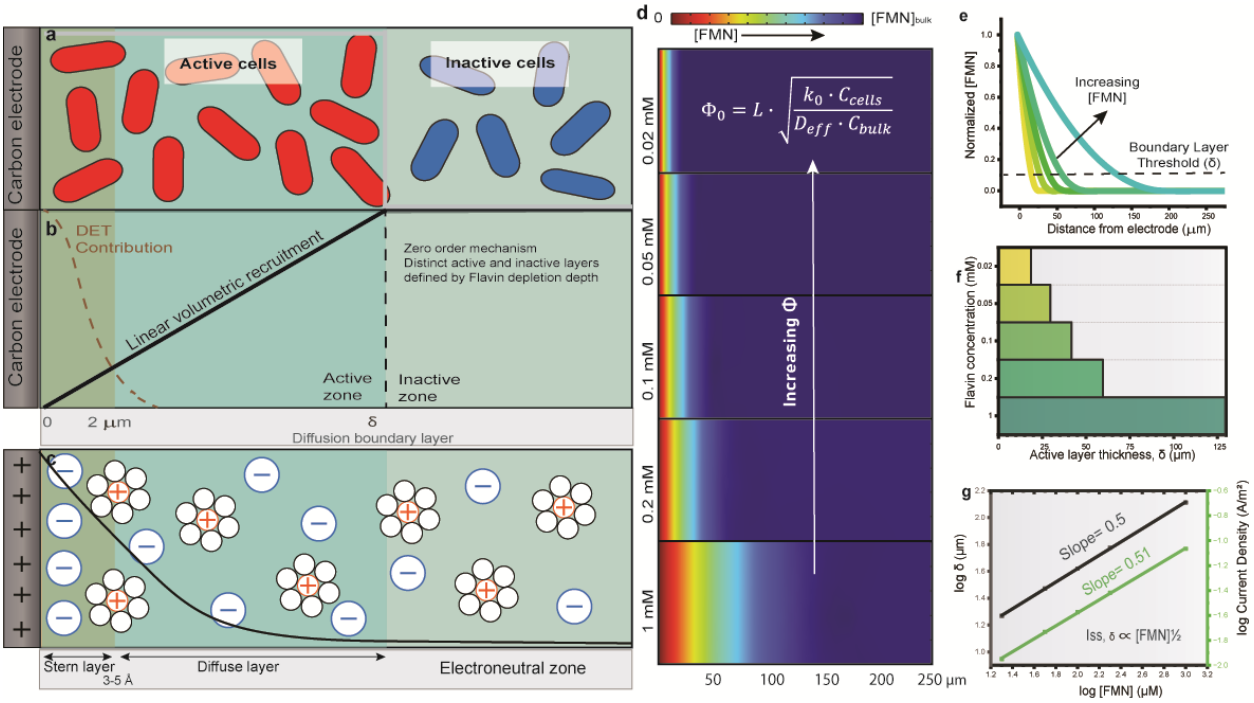
aqueous/hydrogel media is exceptionally rapid ($D_{H^+} \approx 9 \times 10^{-5}$ cm^2/s, aided by the Grotthuss mechanism) relative to the bulkier flavin shuttles ($D_{FMN} \approx 10^{-6}$ cm^2/s), and given adequate electrolyte buffering capacity, local pH accumulation is assumed to be negligible compared to the primary diffusion limitations of the shuttle species itself[31,32]. Under unbuffered or extreme current density regimes, these proton gradients could act as an additional transport resistance, presenting a valuable avenue for future model extensions.

Macroscopic Continuum Modeling and the Square-Root Flavin Scaling Regime

The basic question we sought to answer here is: how do localized kinetics scale to dictate macroscopic charge translocation in biofilms? In both natural biofilms and engineered hydrogels, DET decreases precipitously within roughly 2 μm of the electrode surface[4] (**Figure 2a,b**). To establish a physically intuitive framework for this spatial transition, inspiration was taken from classical interfacial electrochemistry and the Stern model of the electric double layer[33,34] (**Figure 2c**). Just as an electrified interface partitions charge into a compact, rigidly adsorbed Stern layer and an extended mobile diffuse layer, the three-dimensional electromicrobial matrix can be seen as organizing into two distinct charge-transport regimes[35,36] (**Figure 2b,c**). At the electrode interface ($x \leq 2$ μm), a fixed, close-packed cellular monolayer operates as a "biological Stern layer," where electron transfer occurs exclusively via direct outer-membrane cytochrome contact (**Figure 2b,c**). Much like the Stern layer in classical electrochemistry, this region rapidly saturates and imposes a strict geometric ceiling that prevents outward expansion[21] (**Figure 2a,b**). Extending beyond this interfacial regime to the active boundary layer thickness (δ), the matrix functions as a "biological diffuse layer," wherein mediators drive charge translocation across a reaction-diffusion continuum[37] (**Figure 2b,c**). At distances larger than the active boundary layer thickness, severe mediator depletion effectively renders the bulk matrix functionally electroneutral where there is no net

current generation[13] (**Figure 2a-c**). To bridge the gap between single-cell metabolic rates and bulk device performance, we developed a continuum macro-scale transport model that volume-averages discrete bacterial cells into a continuous, reactive matrix domain to capture the impact of shuttle diffusion on spatial segregation between active (red) and inactive (blue) biomass (**Figure 2a**).

Figure 2: Continuum macro-scale transport modeling and zero-order square-root scaling regime.



a, Spatial segregation of a 3D electromicrobial matrix into metabolically active (red) and substrate-starved/inactive (blue) cell populations. **b**, Active layer thickness (δ) demarcation defining the boundary where volumetric recruitment transitions to diffusion-limited depletion. **c**, Interfacial charge transport and electric double-layer structure across the matrix domain. **d**, Simulated 2D spatial concentration heatmaps of oxidized flavin mononucleotide (FMN_{ox}) across varying Thiele modulus (Φ_0) regimes. **e**, Normalized FMN_{ox} concentration decay profiles extending from the working electrode interface ($x = 0$), where the dashed line denotes the boundary layer threshold (δ). **f**, Calculated active layer thickness (δ) as a function of bulk FMN_{ox}concentration. **g**, Log-log scaling relationship of active layer thickness (δ, black) and steady-state current density (I_{ss}, green) versus bulk FMN_{ox}concentration, establishing the $FMN_{ox}^{1/2}$ power-law dependence.

To evaluate this reaction–diffusion interplay in a defined geometry, we constructed a two-dimensional finite-element model in COMSOL Multiphysics representing either a natural biofilm or an engineered bio-hydrogel. The simulation captures the transport domain bounded by a biased anode interface on one side and incorporates volumetric shuttle reduction throughout the matrix. Simulating a broad concentration sweep of bulk flavin ($C_{\text{bulk}} = 0$ to 1.0 mM) revealed a clear spatial restructuring of the internal matrix environment (**Figure 2d**). At low bulk concentrations (0.02-0.05 mM), the bio-anode operates in a high Thiele modulus regime (Φ_0), where local biological consumption severely outpaces diffusive shuttle supply. The two-dimensional spatial concentration heatmaps demonstrate that incoming oxidized flavin is rapidly consumed within the first few micrometers of the electrode interface, creating a narrow active boundary layer (δ) that leaves the majority of interior cells metabolically dormant (**Figure 2a,d**). Increasing the bulk flavin concentration to 1.0 mM drives a continuous decrease in the Thiele modulus, reflecting the progressive alleviation of transport limitations (**Figure 2d**). This downward shift in Φ_0 directly tracks the expansion of the active layer (δ), pushing the flavin penetration front deeper into the hydrogel matrix and progressively recruiting additional biomass into an active metabolic state (**Figure 2a,d**).

To quantitatively evaluate this spatial expansion, we extracted the normalized FMN_{ox} spatial decay profiles ($[FMN_{ox}]/[FMN_{ox}]_{bulk}$) across distance from the electrode interface (**Figure 2e**). Tracking this boundary layer (defines as 90% mediator consumption) across concentration sweeps shows that δ expands systematically from 3.2 μm at 0.02 mM FMN_{ox} up to 25.8 μm at 1.0 mM FMN_{ox} (**Figure 2f**).

When both the active boundary layer thickness (δ) and the total integrated steady-state current density (J_{ss}) were plotted against bulk flavin concentration on a log-log scale, a defined scaling relationship emerged (**Figure 2g**). The simulated log-log trace for current density (J_{ss}, green) yields a linear regression slope of 0.51, while the active layer thickness (δ, black) exhibits an analytical slope of exactly 0.50 (**Figure 2g**). This close agreement (0.51 vs. predicted 0.5) strongly supports the proposed scaling model, indicating that

in zero-order reaction-diffusion matrices, macroscopic current density scales approximately with the square root of bulk mediator concentration ($C_{\text{bulk}}^{1/2}$), consistent with the linear volumetric expansion of the active boundary layer (δ) (**Figure 2b,g**).

This finding represents a significant conceptual advance in the design of bio-electrochemical systems: far from being an intractable mass-transport bottleneck, this square-root scaling relationship acts as a powerful, deterministic design handle for both natural and artificial electromicrobial systems. In natural biofilms, endogenously produced flavin pools are severely limited, typically maintaining concentrations in the low nanomolar range ($0.2 - 1\ \mu M$ [10,16,25]) and trapping the biofilm in a thin, surface-bound active layer (**Figure 2a**). In engineered bio-anodes, flavin loading can be precisely controlled via exogenous addition to concentrations as high as the solubility limit of FMN in aqueous buffer ($100 - 200$ mM in water[38]). This expanded concentration window represents a chemical concentration range of seven orders of magnitude (10^7). When translated using the 0.5 scaling exponent to a predicted generated current, the range expands by more than 1000-fold (10^3). Thus, our understanding of the macroscopic scaling relationship between flavin concentration and current production enables enhanced rational design in which local mediator concentration and retention can be tuned to maximize current generation rather than working to overcome internal mass-transport limits.

Model limitations

To validate the fidelity of our continuum model parameterization and delineate the physical boundaries governing the half-order power-law relationship ($\text{slope} = 0.5$), we performed systematic parametric sensitivity sweeps across key kinetic, transport, and geometric variables (**Figure S3**). These simulations reveal that the characteristic square-root dependence on mediator concentration is not an intrinsic mathematical artifact, but rather emerges exclusively within physically grounded operational regimes characterized by a precise balance between metabolic turnover and mass transport.

Varying $i_{0,\mathrm{ref}}$ across a four-fold range (5 to 20 A/m^2) resulted in identical calculated steady-state current densities (I_{ss}), with all curves collapsing onto the same $C_{\mathrm{ox}}^{1/2}$ scaling relationship. This confirms that the numerical model operates strictly within the mass-transport-limited regime ($Da_{\mathrm{el}} \gg 1$), ensuring that variations in $i_{0,\mathrm{ref}}$ do not artificially constrain the simulated current.

Evaluating the volumetric reaction rate (K_{bio}) demonstrated that high kinetic turnover ($K_{\mathrm{bio}} = 0.1\ \mu$M/s) maintains a robust half-order scaling (slope $= 0.5, R^2 = 1$), confirming a mass-transport-limited regime. Conversely, diminishing K_{bio} (0.01-0.05 μM/s) at elevated mediator concentrations ($\log C_{\mathrm{ox}} > 2.3$) causes the power law to collapse, as biological turnover replaces diffusion as the primary rate-limiting bottleneck. A complementary transition occurs when varying the Michaelis affinity constant (K_m). While low affinity constants (0.5-1.0 μM) sustain the ideal 0.5 logarithmic slope by preserving zero-order metabolic saturation across the tested window, elevated K_m values (5-10 μM) disrupt scaling at low mediator concentrations ($\log C_{\mathrm{ox}} < 2.0$), where the system shifts into sub-saturated, first-order kinetic control ($C_{\mathrm{ox}} \ll K_m$).

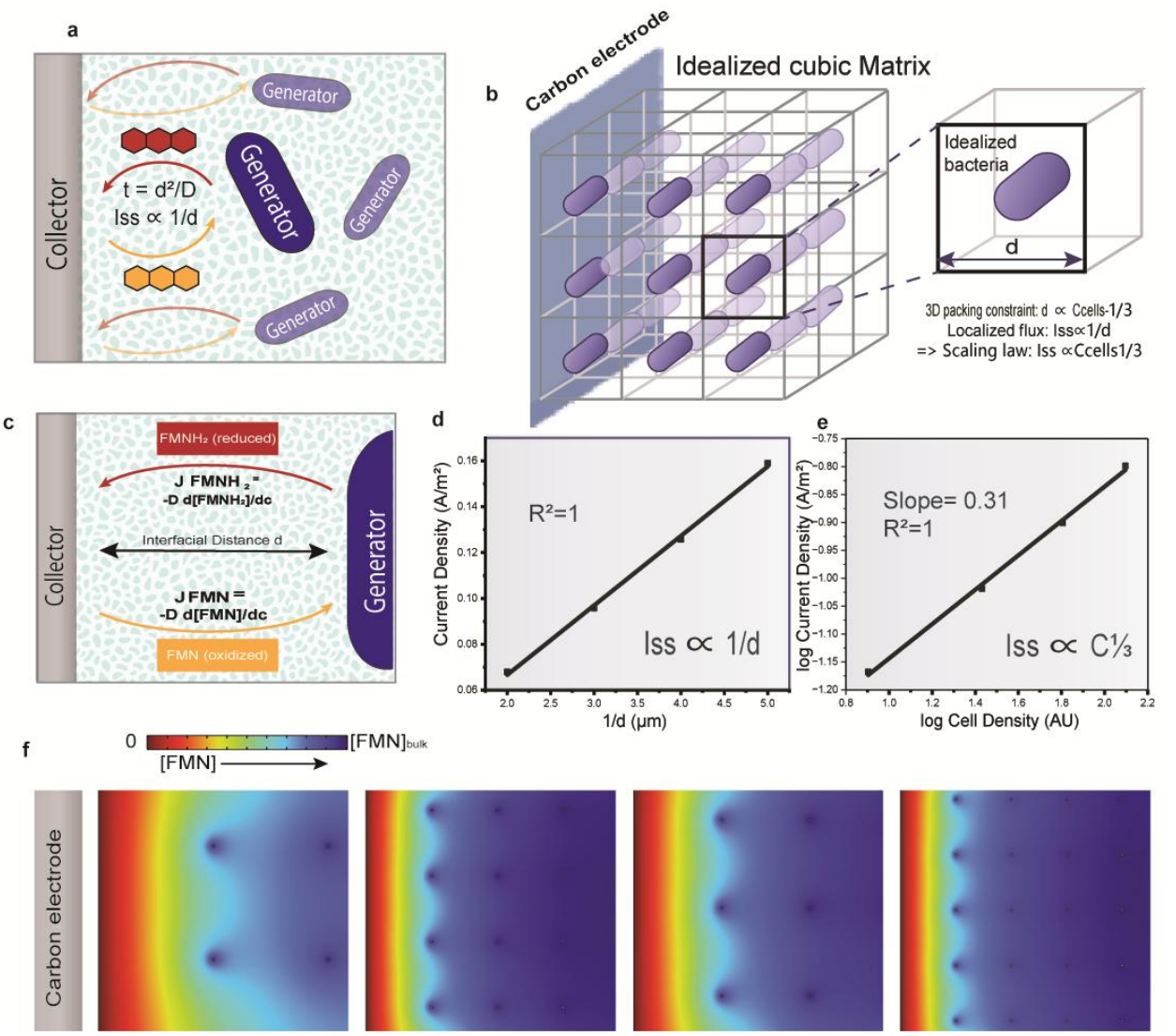
In contrast to kinetic rate parameters, modulating the effective diffusivity ($D_{\mathrm{eff}} = 1 \times 10^{-10}$ to 4×10^{-10} m^2/s) systematically shifted the overall magnitude of the steady-state current density proportional to $\sqrt{D_{\mathrm{eff}}}$ while strictly retaining the invariant 0.5 scaling slope ($R^2 = 1$). This behavior establishes hydrogel diffusional resistance as a pure magnitude-scaling prefactor that operates without perturbing the underlying governing physics at the examined range. Finally, computational sensitivity testing of the transport gap thickness revealed that spatial domains $\geq 375\ \mu$m allow for the uninhibited development of the concentration boundary layer. Restricting the transport gap to 250 μm causes the fixed bulk boundary condition to artificially truncate the developing diffusion layer, thereby breaking the scaling correlation. Collectively, these parametric sweeps confirm that our experimental system operates firmly within the reaction-saturated, transport-limited regime required for half-order catalytic scaling.

To evaluate whether electron donor transport influences metabolic rates within the bio-anode matrix, sodium lactate was supplied at a bulk concentration of 10 mM, well above the half-saturation constant for lactate uptake in *Shewanella oneidensis* ($K_m \approx$ 0.15-0.3 mM[39,40]), maintaining zero-order metabolic uptake kinetics[8]. At maximum steady-state current density ($j_{\max}$), the required stoichiometric lactate consumption rate for four-electron oxidation to acetate ($r_{\text{lac}} = \frac{j_{\max}}{4Fd}$[8]) is over 15-fold lower than the maximum Fickian diffusive flux through the 500 µm hydrogel layer ($J_{\text{diff}} = \frac{D_{\text{lac}} C_{\text{bulk}}}{L}$, assuming $D_{\text{lac}} \approx 1.0 \times 10^{-9}$ m^2/s[13]). Furthermore, within the narrow active boundary layer (δ_{act}), the dimensionless Thiele modulus for lactate ($\phi_{\text{lac}} = \delta_{\text{act}} \sqrt{\frac{k}{D_{\text{lac}}}} \ll 1$[4]) confirms that lactate transport operates deep in the kinetically controlled regime with negligible spatial concentration gradients. Consequently, electron donor supply remains unlimiting throughout the matrix, justifying the single-species focus on mediator diffusion-reaction kinetics.

Microscopic Mechanistic Origin of the $\mathbf{1/3}$ Scaling Exponent via Distributed 3D Redox Cycling

Having established a model describing the bulk mediator availability, we next sought to understand the role of micro-scale cellular packing density in localized charge transport. While volume-averaged continuum models successfully predict bulk concentration profiles, short-range transport physics occurring between individual microbial cells are lost at this scale. We therefore transitioned to a spatially resolved, discrete micro-scale model. By explicitly resolving individual bacteria as distinct boundary-reactive geometries arranged within an idealized three-dimensional cubic lattice, we mapped the influence of microbial density on local diffusion fields (**Figure 3a,b**).

Figure 3: Discrete micro-scale transport modeling and the origin of the $C_{\text{cells}}^{1/3}$ biomass scaling law.



a, Micro-scale model of distributed bacterial "generators" driving local redox cycling with the global collector electrode. **b**, Schematic of an idealized 3D cubic lattice defining inter-cellular spacing (d) governed by 3D packing constraints ($d \propto C_{\text{cells}}^{-1/3}$). **c**, Interfacial flux equilibrium between oxidized ($J_{\text{FMN}_{\text{ox}}}$) and reduced ($J_{\text{FMNH}_2}$) shuttles across inter-cellular distance d. **d**, Direct linear relationship between steady-state current density (I_{ss}) and inverse inter-cellular distance ($1/d$, $R^2 = 1$). **e**, Log-log plot of simulated current density versus cell packing density (C_{cells}), yielding a numerical slope of $0.31 \approx 1/3$ ($R^2 = 1$). **f**, COMSOL 2D finite-element spatial concentration profiles of oxidized FMN around individual cell boundaries, depicting the transition from isolated diffusion fields to cooperative, overlapping fields with increasing cell density.

Just as classical electrochemical theory served as inspiration for the macroscopic MET model, we employed the theory behind electrochemical redox cycling in interdigitated microelectrode arrays to model local

mediator cycling at the microscale (**Figure 3a**). In a traditional two-electrode generator-collector cell, current is sustained by continuous shuttle recycling between oppositely-polarized adjacent electrodes, where the characteristic diffusion time scales as $t = d^2/D$ and the steady-state flux scales inversely with the inter-electrode gap ($I_{ss} \propto 1/d$)[41–43]. In our three-dimensional biological adaptation, the planar carbon electrode acts as a global electron collector held at an oxidizing potential, while the surrounding microbial cells function as microscopic generators that continuously reduce oxidized mediator at a zero-order rate (**Figure 3a,c**). Here, the characteristic distance d defines the localized interfacial transport gap separating individual generators (bacterial cells) from the collector interface (the carbon electrode), across which FMN_{ox} and $FMNH_2$ undergo counter-directional Fickian diffusion (**Figure 3c**).

The geometric link between macroscopic cell density (C_{cells}) and this localized transport length (d) is rooted in three-dimensional Euclidean space. Within an assumed uniform cubic packing arrangement, the unit volume allocated per cell scales as $V \propto d^3$. Because volumetric cell concentration is inversely proportional to this unit cell volume ($C_{cells} \propto 1/V$), the physical spacing between neighboring microbial centers scales inversely with the cube root of biomass density ($d \propto C_{cells}^{-1/3}$) (**Figure 3b**). Combining the geometric constraint of an average electrode-to-cells distance with the short-range diffusive shunting flux ($I_{ss} \propto 1/d$) yields the theoretical micro-scale scaling law: $I_{ss} \propto C_{cells}^{1/3}$.

Extracting the net steady-state current density (I_{ss}) from the discrete finite-element simulations provides quantitative validation of this model. Plotting I_{ss} directly against inverse inter-cellular distance ($1/d$) yields a perfectly linear relationship ($R^2 = 1.0$), confirming that short-range diffusive shunting is the direct driver of cell density-dependent current enhancement (**Figure 3d**). When viewed in macroscopic engineering terms by plotting $\log I_{ss}$ against $\log C_{cells}$, linear regression yields a numerical scaling exponent of 0.31 with $R^2 = 1.0$ (**Figure 3e**).

The minor divergence between the simulated exponent (0.31) and the idealized theoretical prediction (0.33) reflects two physical realities captured by the discrete model. First, bacteria situated immediately adjacent to the planar carbon anode experience an asymmetric, semi-infinite diffusion boundary compared to cells within the active diffusion layer. Second, because real bacteria occupy finite physical volume rather than acting as infinitesimal point sinks, a non-negligible fraction of the unit cell volume is occupied by biomass, slightly altering the effective fluid gap available for mediator diffusion.

To visualize this geometric transport coupling, we simulated steady-state flavin concentration profiles across a range of cell packing densities (**Figure 3f**). The spatial concentration fields reveal a clear transition between micro-transport regimes. At low cell densities (large electrode-cells distance d), localized depletion zones around individual bacteria remain completely isolated, displaying classic hemispherical diffusion profiles (**Figure 3f, left**). As the density of bacteria increases and inter-cellular spacing decreases, neighboring depletion fields strongly overlap, demonstrating cooperativity (**Figure 3f, right**). In this densely packed regime, mass transport within the matrix is dominated by rapid, short-range diffusive recycling between adjacent cells and the surrounding fluid, enabling the full volume of the biofilm or hydrogel to serve as an efficient three-dimensional redox cycling engine. These micro-scale insights demonstrate that the $1/3$ power law is a fundamental physical consequence that emerges when localized 3D redox cycling operates within the cubic packing limits of dense living architectures.

Finally, integrating our microscopic and macroscopic transport models enables the mapping of the full reaction-diffusion landscape on a three-dimensional parametric response surface (**Figure S4**). This global current map illustrates how macroscopic current output (I) varies across simultaneous variations in bulk flavin loading ($[\mathrm{FMN_{ox}}]$) and cellular packing density (C_{cells}). Ultimately, this multiscale framework demonstrates how microscopic geometry and macroscopic transport physics converge to dictate bio-electrochemical performance. By coupling the localized Euclidean packing constraints ($I_{\mathrm{ss}} \propto C_{\mathrm{cells}}^{1/3}$) that drive short-range 3D redox cycling with continuum reaction–diffusion mechanics ($I_{\mathrm{ss}} \propto C_{\mathrm{bulk}}^{1/2}$) across the

hydrogel matrix, this unified model accounts for multi-order-of-magnitude variations in current density as a function of key process parameters.

Empirical Validation with Artificial Biofilms

For our theoretical transport models to be useful to bio-electrochemical system design, they must be shown to hold true under experimental conditions. We therefore fabricated synthetic, self-contained artificial biofilms by co-encapsulating *S. oneidensis* MR-1 bacteria, exogenous Flavin Mononucleotide (FMN), soldium lactate as a carbon source, and essential metabolic nutrients within an agarose hydrogel matrix (**Figure 4a**). To prevent heat-shock induction and loss of viability beyond the organism's optimal 30°C physiological threshold[44,45], the cells were encapsulated using Low Melting Point Agarose, enabling cell entrapment at low processing temperatures (~30°C). These agarose hydrogels were mounted directly onto planar, screen-printed carbon electrodes in a three-electrode setup to enable precise control over FMN concentration and cell density while avoiding the inherent heterogeneity and slow growth dynamics of natural biofilms (**Figure 4a,b**). Unless otherwise specified, baseline characterizations were conducted under standard reference conditions: a 1% w/v agarose matrix, 100 μM bulk FMN_{ox} loading, and an encapsulated cellular density of 8 equivalent OD_{600} (8 $OD_{600,eq}$), with each experiment altering a single variable while holding the remaining two constant. Live-cell fluorescence microscopy using SYTO 9 staining confirmed high post-encapsulation cellular viability and a spatially homogeneous bacterial distribution throughout the hydrogel matrix (Figure 4c). The living cells were shown to take up ~0.02% of the total volume of the matrix, which corresponds to the cell density assumption of $0.5 - 1 \cdot 10^9$ S. Oneidensis cells/ml per OD_{600} unit[46,47] (**Figure 4d**).

To verify that current generation stems strictly from active bacterial metabolism, living hydrogel bio-anodes containing wild-type (WT) *S. oneidensis* MR-1 or the flavin-export-deficient Δbfe mutant were compared against dead-cell and cell-free controls (**Figure 4e**). Across both 200 μM and 1000 μM exogenous FMN

conditions, living-cell formulations produced robust current densities, whereas dead-cell and cell-free controls yielded near-zero baseline currents ($\sim 0.001\ \mathrm{A\ m^{-2}}$, $p < 0.001$). At 200 μM FMN, average current densities reached $0.036\ \mathrm{A\ m^{-2}}$ for WT and $0.045\ \mathrm{A\ m^{-2}}$ for Δbfe, rising to $0.077\ \mathrm{A\ m^{-2}}$ and $0.094\ \mathrm{A\ m^{-2}}$ at 1000 μM FMN ($p < 0.01$; **Figure 4e**). The modest enhancement in current density observed for the Δbfe mutant is attributed to cellular energy and cofactor conservation. Because the hydrogel matrix already contains abundant exogenous FMN to saturate outer-membrane MtrC/OmcA cytochromes, deleting the Bfe transporter (SO_0702) eliminates the energetic cost and cofactor loss associated with active flavin export, enabling the cells to direct more metabolic energy toward respiratory electron discharge[3].

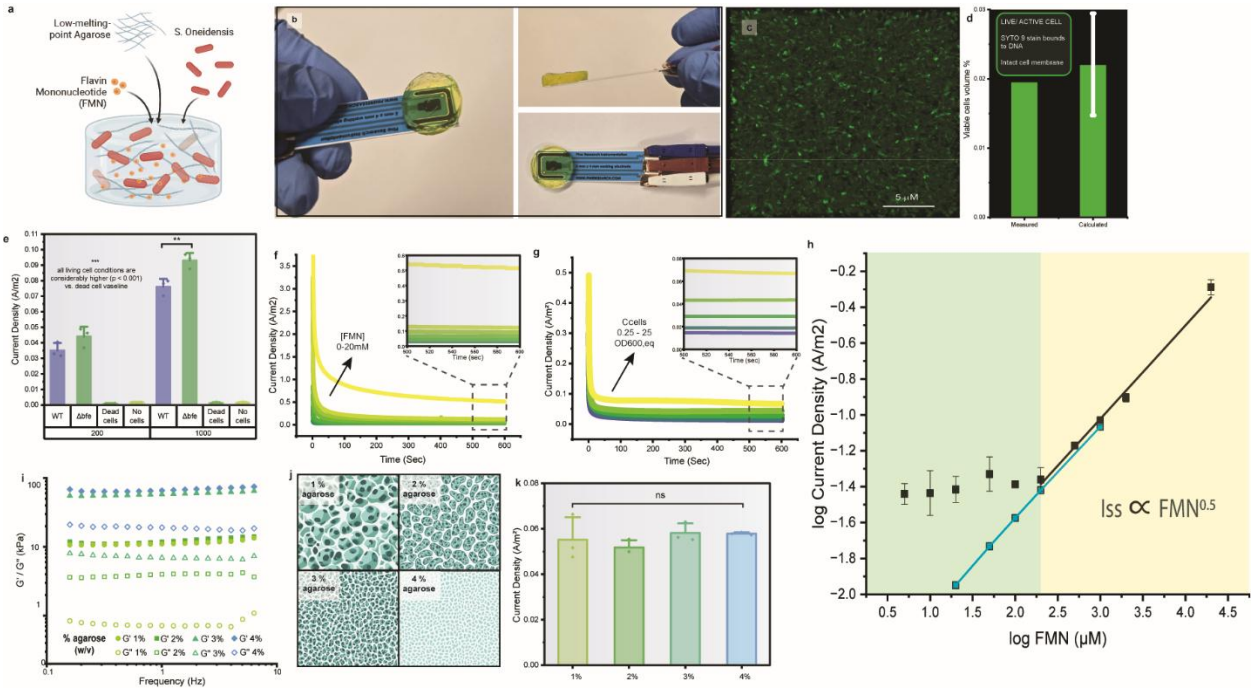


Figure 4: Empirical validation and mechanical-transport decoupling in encapsulated artificial biofilms. a, schematic of fabricating cell-encapsulated agarose hydrogel bio-anodes. **b** Photographs of the 3D hydrogel bio-anode mounted on a three-electrode electrochemical chip**, c,** Confocal live-cell fluorescence micrograph of SYTO 9-stained *S. oneidensis* distributed within a 1% (w/v) agarose matrix (scale bar, 5 µm). **d,** Comparison of measured and calculated viable cell volume percentage (% v/v) within the hydrogel matrix.. **e,** Control experiment of steady-state current density comparing wild-type (WT), Δ*bfe* mutant, heat-killed dead cells, and cell-free control at 200 µM and 1000 µM FMN (P < 0.001, *P < 0.01). **f**, Chronoamperometric current traces across bulk FMN concentrations (0–20 mM). Inset highlights the

steady-state evaluation window (500–600 s). **g,** Chronoamperometric current traces across cell densities (Ccells = 0.25-25 $OD_{600,eq}$). Inset highlights the steady-state evaluation window (500–600 s). **h,** Logarithmic plot of steady-state current density (Iss) as a function of FMN concentration, demonstrating power-law scaling (Iss $\propto$ $FMN^{0.5}$) for experimental and computational current densities. **i,** Oscillatory shear rheology frequency sweeps displaying storage (G', filled) and loss (G'', open) moduli for 1% to 4% (w/v) agarose hydrogels. **j,** Schematics of hydrogel microstructures across 1%-4% (w/v) agarose concentrations (adapted from Trudicova et al.[48]). **k,** Measured steady-state current density (Jss) across 1%-4% (w/v) agarose matrix concentrations (ns, not significant), demonstrating mechanical-transport decoupling. Error bars represent standard error of the mean (SEM).

To isolate the contribution of exogenous flavin without risking interference from endogenous secretion, all subsequent experimental characterization (**Figures 4f-k**) was performed exclusively using the Δbfe strain. Continuous 10-minute chronoamperometry traces were recorded at an applied anodic bias of $+0.4$ V vs. an integrated quasi-reference Ag/AgCl electrode, a potential sufficiently higher than the formal oxidation potential of FMN to ensure complete, mass-transport-limited mediator oxidation at the carbon electrode interface. Across a range of FMN_{ox} concentrations (0-20 mM) (**Figure 4f**) and cell densities (0.25-25 $OD_{600,eq}$) (**Figure 4g**), currents generated from the system exhibited rapid equilibration to stable steady-state plateaus after an initial transient decay. Steady-state current densities (I_{ss}) were calculated based on the time average over the final 100 seconds ($t = 500$-600 s) of each polarization run (**Figure 4f,g insets**).

To elucidate the transport and kinetic scaling behavior governing shuttle-mediated electron transfer, steady-state current density (I_{ss}) was evaluated across a broad spectrum of exogenous FMN concentrations (5 μM to 20 mM) in log-log scale (**Figure 4h**). Experimental results revealed two distinct operational regimes. At elevated mediator concentrations ($[FMN_{ox}] \geq 200$ μM), steady-state current density exhibited a half-order power-law scaling relationship, $I_{ss} \propto [FMN_{ox}]^{0.5}$, reflected by a linear slope of 0.5 in log-log coordinates (**Figure 4h**). Conversely, at lower mediator concentrations ($[\mathrm{FMN}] < 200$ μM), current generation decoupled from shuttle concentration, reaching a constant, concentration-independent plateau at approximately $\log I_{ss} \approx -1.4$ A m^{-2} (~ 0.04 A m^{-2}; **Figure 4h**). Overlaying the finite element COMSOL

model predictions (derived as elaborated in the methods section; blue curve) demonstrated strong quantitative agreement with experimental currents within the high-concentration regime (**Figure 4h**).

The observed discrepancy between the raw continuum model predictions and experimental current measurements (**Figure 4h**) arises from a combination of structural, transport, and biological factors that deviate from idealized theoretical assumptions. First, imperfect physical contact at the hydrogel–electrode interface, caused by microscopic surface roughness, localized microgaps, and hydrogel detachment, substantially reduces the effective electrochemical surface area compared to the theoretical contact area[49,50]. Second, solute transport within the crosslinked polymer network experiences steric hindrance and increased tortuosity, resulting in an effective diffusion coefficient lower than the theoretical value in pure aqueous solution[51,52]. Third, the maximum biological reaction rate (v_{bio}) under experimental conditions may fall below theoretical kinetic limits due to localized mass-transport limitations, substrate depletion micro-environments, and cell metabolic stress within the matrix[21]. Together, these physical and biological constraints account for the lower observed current density and justify the empirical scaling factor applied to align continuum predictions with experimental data.

The continuum model maintained a strict linear log-log slope across the entire concentration range, failing to capture the experimental current plateau observed at low shuttle loadings (**Figure 4h**). The 0.5 power-law scaling exponent confirms that at higher mediator loadings, bio-anode performance is governed by a classic reaction–diffusion boundary layer, where current generation is co-limited by species diffusion (D_{eff}) and volumetric biological turnover within the hydrogel matrix[28]. The inability of the COMSOL model to capture the low-concentration current plateau highlights secondary mechanisms that become dominant when soluble shuttle availability is scarce. First, physical contact between outer-membrane cytochromes (MtrC/OmcA) on bacteria situated directly at the hydrogel–electrode interface can sustain a baseline current via direct electron transfer (DET), operating independently of soluble shuttle diffusion[53,54]. Second, the computational model assumes that K_m is negligible relative to local shuttle availability ($c_{\mathrm{Ox}} \gg K_m$) within

Equation 2. At low micromolar FMN_{ox} levels, this assumption breaks down as mediator concentrations approach or fall below K_m. Under these conditions, localized non-linear enzyme saturation dynamics and cofactor recycling deviate from the simplified rate law in Equation 2, sustaining a steady baseline current that pure continuum diffusion models underpredict.

Furthermore, across cell densities (0.25-25 $OD_{600,eq}$), a monotonic increase in current is observed, as is a clean log-log linear fit ($R^2 = 0.99$) with an empirical power-law exponent of 0.32 (Supplementary **Figure S5a**). This value closely matches our discrete simulation (0.31, **Figure 3d**) and approaches the theoretical $1/3$ power law (0.33), confirming that the inter-cellular spacing ($d \propto C_{\text{cells}}^{-1/3}$) controls the three-dimensional redox cycling kinetics in active bio-matrices. Together, these empirical observations validate our theoretical framework as a fully predictive design model for engineering high-performance bio-electrodes.

Crucially, by optimizing biomass density and mediator loading (20 mM FMN_{ox}), our artificial biofilm platform achieved steady-state current densities exceeding 0.5 A m^{-2} on standard, un-functionalized screen-printed carbon electrodes (**Figure 4h-j**). This benchmark represents a major milestone, significantly surpassing the maximum current densities reported for conventional, un-supplemented two-dimensional planar bio-anodes 0.01-0.25 A m^{-2}). By unlocking three-dimensional transport enhancements through controlled mediator diffusion, we eliminate the geometric surface area constraints conventionally thought to apply to biofilms on electrodes. This approach further enables the use of inexpensive carbon supports for highly efficient bio-electrochemical systems[55–58].

Decoupling Hydrogel Mechanics from Mass Transport

Finally, we evaluated how varying the hydrogel matrix concentration ($1 - 4\%$ w/v agarose) impacts both macroscopic mechanical rigidity and electrochemical performance in artificial biofilms encapsulated with the Δbfe strain at standard reference loading ($100\ \mu$M FMN_{ox}, 8 $OD_{600,eq}$) (**Figure 4i-k**). Oscillatory

shear frequency sweeps (0.1-6.5 Hz) demonstrate solid-like hydrogel behavior across all formulations, with the elastic storage modulus (G') consistently dominating the viscous loss modulus (G'')[59] (Figure 4i). Increasing agarose concentration led to a corresponding increase in G' from 10.2 kPa at 1% agarose to 74.8 kPa at 4% agarose, providing nearly an order of magnitude range in mechanical stiffness that is compatible with electroactive microbes[60]. This window is compatible with diverse processing techniques such as extrusion bioprinting or structural casting[61,62].

Remarkably, despite this substantial variation in macroscopic stiffness and the corresponding microstructural densification of the hydrogel network (**Figure 4j**), the steady-state current density (I_{ss}, evaluated at $t = 500\text{-}600$ s) remained statistically invariant across all formulations ($p > 0.05$, non-significant; **Figure 4k**). We attribute this complete mechanical-electrochemical decoupling to the multiscale pore architecture of the agarose matrix. Even at 4% w/v concentration, the average pore radius of the hydrogel network ($r_{pore} \approx 100\text{--}300$ nm)[63] remains orders of magnitude larger than the hydrodynamic radius of the flavin mononucleotide shuttle ($r_{h,\,FMN} \approx 0.8$ nm). In accordance with stochastic mesh obstruction models[51,64] and empirical macromolecular transport studies in agarose matrices[52], significant diffusional retardation occurs only when the solute radius approaches the nanometer-scale mesh spacing ($r_h > 30$ nm). Consequently, local steric resistance and microscale electrostatic interactions experienced by diffusing FMN molecules remain virtually identical across the investigated density regime. This decoupling enables independent tuning and optimization of hydrogel mechanical properties for bio-fabrication without introducing mass-transport penalties or sacrificing catalytic current output.

Discussion

The transition from two-dimensional surface attachment to three-dimensional volumetric bio-electrodes has long been impeded by severe mass-transport limitations that leave deep cellular architectures

metabolically inactive. By establishing a unified multi-scale transport framework, this work resolves the fundamental trade-off between mediator availability and cellular kinetics. Our model demonstrates that three-dimensional charge transport in electromicrobial systems is governed by two complementary power-law scaling regimes: a macroscopic continuum regime where active layer expansion scales with the square root of bulk mediator loading ($I \propto C_{\text{bulk}}^{1/2}$), and a microscopic regime where local flux scales with the cube root of cellular packing density ($I \propto C_{\text{cells}}^{1/3}$). Empirical validation using engineered *Shewanella oneidensis* hydrogels confirms that these physical scaling laws predictably drive steady-state current generation across orders of magnitude, breaking the performance ceilings imposed by traditional planar monolayer architectures. Crucially, matrix stiffness and diffusive charge transport are functionally decoupled within these porous networks. Elasticity can be varied across an order of magnitude without transport penalties, enabling independent structural optimization for 3D bioprinting, bio-manufacturing, and flow-reactor design.

Looking forward, this multi-scale framework advances research along two distinct trajectories: decoding natural microbial ecosystems and engineering optimized bio-hybrid systems. First, it offers microbial ecologists a mechanistic lens to unravel internal transport architectures, spatial segregation, and metabolic dynamics within complex, natural multispecies biofilms. Second, it equips bio-engineers with a quantitative blueprint to advance both biosensing and bio-energy technologies. By explicitly linking measured current output to active cellular concentration, this model provides the theoretical foundation required for precise analytical signal transduction in bacterial-based sensors. Simultaneously, to maximize current and power generation for bio-energy applications, these scaling laws outline clear material design rules: optimizing matrix structures and mediator selection to achieve higher effective diffusion coefficients, alongside maximizing mediator loading up to its solubility limit. Finally, building upon this continuum model, incorporating electrochemical impedance spectroscopy (EIS) modeling will offer finer mechanistic resolution into the dynamic transition between direct electron transfer (DET) and mediated

electron transfer (MET) at the cellular–electrode interface, an avenue we are actively pursuing in follow-up research.

Methods

Finite Element Method (FEM) Computational Modeling

Two-dimensional transient continuum models were implemented in COMSOL Multiphysics (v6.3) using the Transport of Dilute Species and Electrochemistry modules.

Macro-Scale Continuum Model: The hydrogel was modeled as a rectangular spatial domain (Gap $=$ $500\ \mu$m, $H = 100\ \mu$m). Species transport was governed by Nernst–Planck diffusion ($D_{\text{eff}} = 4 \times 10^{-10}$ m^2/s). Volumetric mediator reduction by encapsulated biomass was defined by Michaelis–Menten kinetics ($k_{\text{bio}} = 50\ \mu$M/s, $K_m = 1\ \mu$M) for a two-electron reduction with smoothed Heaviside lower-bound constraints (flc2hs):

$$R_{\text{cOx}} = -k_{\text{bio}} \left(\frac{c_{\text{Ox}}}{K_m + c_{\text{Ox}}} \right) \cdot \text{flc2hs}(c_{\text{Ox}}, 10^{-9})/2$$

Heterogeneous electron transfer at the working electrode ($x = 0$) followed concentration-dependent Butler–Volmer kinetics ($I_{0,\text{ref}} = 10$ A m^{-2}, $V_{\text{anode}} = +0.4$ V vs. Ag/AgCl, $E_{\text{eq,FMN}} = -0.422$ V). Bulk boundary conditions ($x =$ Gap) held c_{Ox} and c_{Red} constant.

Micro-Scale Continuum Model: Explicit bacterial geometry was resolved using a $320 \times 200\ \mu$m domain containing circular cutouts ($r_{\text{cell}} = 0.5\ \mu$m). Volumetric kinetics were zeroed ($R_i = 0$), and metabolic turnover was assigned exclusively to cell perimeter boundaries as a surface flux condition ($k_{\text{surf}} = 0.465$ mM/(m$^2 \cdot$ s), $K_m = 1\ \mu$M) assuming two electrons are required to reduce each flavin molecule:

$$-\mathbf{n} \cdot \mathbf{J}_{\mathrm{cOx}} = -k_{\mathrm{surf}} \cdot \left(\frac{\max(10^{-9}, c_{\mathrm{Ox}})}{K_m + \max(10^{-9}, c_{\mathrm{Ox}})} \right) / 2$$

Model Parametrization: All physical transport coefficients ($\boldsymbol{D}_{\mathrm{eff}}$), catalytic kinetic rate parameters ($\boldsymbol{k}_{\mathrm{bio}}$, $\boldsymbol{K_m}$), and structural dimensions utilized in both macro- and micro-scale continuum formulations were grounded in independently measured physical properties and established literature precedents. A complete tabulation of parameter values, physical definitions, units, and literature references is detailed in Table S1 of the Supplementary Information.

Discretization and Solvers: Both domain geometries were discretized using unstructured triangular meshes with boundary-layer refinement along the electrode interface and circular cell perimeters. Time-dependent problems were solved using COMSOL's implicit BDF algorithm ($t = 0$-600 s, $\Delta t = 0.1$ s) with a relative error tolerance of 10^{-3}.

Current Output Calculation and Interfacial Contact Scaling: The net current density was determined by integrating the local normal current flux density across the working electrode boundary and dividing by the total electrode surface area. Steady-state current density (I_{ss}) was extracted at $t = 600$ s to mirror experimental measurement durations. To enable direct comparison between continuum model simulations and physical measurements, calculated current values were scaled by an empirical factor of 0.1. This factor accounts for incomplete physical contact at the hydrogel–electrode interface, corresponding to an effective contact area of $\sim 10\%$ resulting from microscopic interfacial roughness, microgap formation, and localized hydrogel detachment along the soft polymer–solid conductor junction[28].

Media and Reagents Preparation

Basal M1 minimal medium was prepared by dissolving 50 mM PIPES (15.12 g/L), 7.5 mM NaOH (0.30 g/L), 28 mM NH_4Cl (1.5 g/L), 1.3 mM KCl (0.10 g/L), 4.3 mM $NaH_2PO_4 \cdot H_2O$ (0.59 g/L), and 100 mM NaCl (5.84 g/L) in double-distilled water (ddH_2O). The solution was adjusted to pH 7.4 and autoclaved. Post-autoclaving, the basal medium was supplemented with sterile-filtered $1000\times$ vitamin

stock, 100 × amino acid stock, and 100 × trace mineral stock at 10 mL/L each. Sodium lactate was added to a final concentration of 10 mM as a carbon source.

Bacterial Cultivation and Cell Density Normalization

Shewanella oneidensis wild-type MR-1 and the flavin-export-deficient Δbfe mutant were maintained as -80°C glycerol stocks. Strains were streaked onto Luria–Bertani (LB) agar plates and incubated at 30°C. A single isolated colony was inoculated into liquid LB medium and grown overnight at 30°C with aerobic shaking at 200 rpm to reach stationary phase. Cells were harvested by centrifugation ($4{,}500 \times g$, 8 min, 4°C), the supernatant was decanted, and the resulting pellet was washed twice in sterile M1 medium.

Biomass loading within the gel matrix was standardized using equivalent optical density ($OD_{600,eq}$). Washed cell suspensions were measured for optical density at 600 nm (OD_{600}) on a UV-Vis spectrophotometer. Total biomass was calculated according to:

$$OD_{total} = OD_{600,harvest} \cdot V_{harvest} = OD_{600,eq,target} \cdot V_{gel}$$

where $V_{gel} = 4$ mL per well. The harvested pellet was resuspended in sterile M1 medium to twice the target final density ($2 \times OD_{600,eq}$) to facilitate 1: 1 (v/v) dilution with matrix precursors.

Dead cells

Heat-killed cell controls were prepared by incubating harvested wild-type Shewanella oneidensis MR-1 cell suspensions in 65 °C for 2 h[10,54]. Following thermal inactivation, the cells were collected by centrifugation ($4500 \times g$, 8 min), washed twice with M1 minimal media, and concentrated. The heat-killed biomass was then incorporated into the agarose hydrogel matrix following the standard encapsulation protocol, maintaining a final cell density equivalent to $OD_{600} = 8.0$.

Bio-Anode Matrix Rationale, Synthesis, and Assembly

To address the critical need for a consistent and reproducible system in electroactive microbe-based bioelectrochemical processes, living bio-anodes were engineered to yield a uniformly distributed cell matrix while preserving cell viability. To preserve cellular viability and physiological functionality during matrix encapsulation, IBI Low Melting Point Agarose was selected over standard agarose formulations. *Shewanella oneidensis* MR-1 exhibits a narrow mesophilic temperature range, reaching peak metabolic activity between 28°C and 30°C while suffering severe growth drop-offs and thermal stress as temperatures approach or exceed 35°C[44,45]. Standard agaroses require mixing temperatures well above this critical threshold, risking thermal inactivation and disruption of respiratory protein machinery. In contrast, low-melting-point agarose remains fluid at lower temperatures ($\sim 30°C$) prior to gelation, enabling homogeneous cell entrapment within a thermally safe window. This low-temperature processing avoids heat shock, ensuring that encapsulated *S. oneidensis* cells maintain high viability, active metabolism, and respiratory performance post-immobilization.

Low-melting-temperature agarose was dissolved in M1 medium at $2\times$ target concentration (2%-8% w/v) and thermally maintained in a liquid state at $> 30°C$. Concentrated $2\times$ bacterial suspensions were mixed 1:1 (v/v) with the warm agarose solution, exogenous Flavin Mononucleotide (FMN, 0-20 mM), and nutrients. Standard baseline hydrogels contained 1% w/v agarose, 100 μM bulk FMN, and an encapsulated cell loading of 8 $OD_{600,eq}$.

Four milliliters (4 mL) of the precursor mixture was poured into each well (34 mm diameter) of a 6-well plate inside a Coy anaerobic chamber ($5\%\ H_2, 20\%\ CO_2, 75\%\ N_2$). Physical crosslinking occurred during room-temperature cooling. After 3 h of anaerobic acclimation, 12 mm diameter hydrogel disks were excised with a circular punch and mounted directly onto un-functionalized planar screen-printed carbon electrodes (Pine Research Instrumentation).

Electrochemical characterization

All electrochemical measurements were conducted inside an anaerobic glove box (Coy Laboratory Products) maintained under a $5\%\ H_2, 20\%\ CO_2, 75\%\ N_2$ atmosphere to prevent oxygen-mediated electron scavenging. Electrochemical analyses were carried out using a Squidstat potentiostat (Admiral Instruments) interfaced with screen-printed electrodes (Pine Research) containing an integrated three-electrode configuration (carbon working electrode, carbon counter electrode, and Ag/AgCl reference electrode). Chronoamperometry (CA) was performed by applying a constant working potential to drive electron transfer. CA traces were recorded over 600 s for hydrogel matrices containing living *Shewanella oneidensis* MR-1 (wild-type or mutant strains), as well as cell-free and heat-killed control hydrogels. Steady-state current density (I_{ss}) was extracted as an average of $t = 500 - 600$ s from terminal current plateaus. CA experiments were conducted across a range of exogenous FMN concentrations ($5\ \mu$M to 20 mM) and optical cell densities ($OD_{600,eq} = 0.25\text{-}25$). Measured currents were normalized to the nominal geometric surface area of the screen-printed working electrode (4 mm X 5 mm) to express performance as current density (A/m^2).

Confocal microscopy

Bacterial cellular distribution and membrane integrity within the hydrogel matrix were evaluated using confocal laser scanning microscopy. Encapsulated Shewanella oneidensis MR-1 constructs were stained using the LIVE/DEAD BacLight Bacterial Viability Kit (Thermo Fisher Scientific) containing SYTO 9 ($3.34\ \mu$M) in $1\times$ PBS for 15 min in the dark at room temperature, followed by a 15 min wash in PBS. Stained hydrogel samples were transferred to glass-bottom slides and imaged using a Zeiss laser scanning confocal microscope equipped with a $63\times/1.40$ NA oil-immersion objective lens. SYTO 9 (live cells) were excited using 488 nm lasers, respectively, with emission collected in distinct spectral channels. Serial optical Z-stacks were acquired through the construct thickness at a step size of $0.5\text{-}1.0\ \mu$m to reconstruct three-dimensional spatial organization, and percent viability using ImageJ software.

Rheology

Shear rheology tests were performed using a stress-controlled AR-G2 rheometer (TA Instruments, New Castle, DE) with an 8mm parallel plate fixture. All experiments were performed on a Peltier plate at 25 °C. Small amplitude oscillatory shear (SAOS) measurements were performed at a strain amplitude within the linear viscoelastic range

References

1. Malvankar, N. S. *et al.* Tunable metallic-like conductivity in microbial nanowire networks. *Nature Nanotech* **6**, 573–579 (2011).
2. Reguera, G. *et al.* Extracellular electron transfer via microbial nanowires. *Nature* **435**, 1098–1101 (2005).
3. Kotloski, N. J. & Gralnick, J. A. Flavin Electron Shuttles Dominate Extracellular Electron Transfer by Shewanella oneidensis. *mBio* **4**, e00553-12 (2013).
4. Torres, C. I. *et al.* A kinetic perspective on extracellular electron transfer by anode-respiring bacteria. *FEMS Microbiol Rev* **34**, 3–17 (2010).
5. Agee, A., Pace, G., Yang, V., Segalman, R. & Furst, A. L. Mixed Conducting Polymers Alter Electron Transfer Thermodynamics to Boost Current Generation from Electroactive Microbes. *J. Am. Chem. Soc.* **146**, 19728–19736 (2024).
6. Erben, J., Pinder, Z. A., Lüdtke, M. S. & Kerzenmacher, S. Local Acidification Limits the Current Production and Biofilm Formation of Shewanella oneidensis MR-1 With Electrospun Anodes. *Front. Microbiol.* **12**, 660474 (2021).
7. Yu, Y.-Y. *et al.* Three-Dimensional Electrodes for High-Performance Bioelectrochemical Systems. *IJMS* **18**, 90 (2017).
8. Ringeisen, B. R. *et al.* High Power Density from a Miniature Microbial Fuel Cell Using *Shewanella oneidensis* DSP10. *Environ. Sci. Technol.* **40**, 2629–2634 (2006).

9. Song, R.-B. *et al.* Bacteria-Affinity 3D Macroporous Graphene/MWCNTs/Fe_3O_4 Foams for High-Performance Microbial Fuel Cells. *ACS Appl. Mater. Interfaces* **8**, 16170–16177 (2016).
10. Marsili, E. *et al. Shewanella* secretes flavins that mediate extracellular electron transfer. *Proc. Natl. Acad. Sci. U.S.A.* **105**, 3968–3973 (2008).
11. Okamoto, A., Hashimoto, K., Nealson, K. H. & Nakamura, R. Rate enhancement of bacterial extracellular electron transport involves bound flavin semiquinones. *Proc. Natl. Acad. Sci. U.S.A.* **110**, 7856–7861 (2013).
12. Lies, D. P. *et al. Shewanella oneidensis* MR-1 Uses Overlapping Pathways for Iron Reduction at a Distance and by Direct Contact under Conditions Relevant for Biofilms. *Appl Environ Microbiol* **71**, 4414–4426 (2005).
13. Stewart, P. S. Diffusion in Biofilms. *J Bacteriol* **185**, 1485–1491 (2003).
14. Schkolnik, G., Schmidt, M., Mazza, M. G., Harnisch, F. & Musat, N. In Situ Analysis of a Silver Nanoparticle-Precipitating Shewanella Biofilm by Surface Enhanced Confocal Raman Microscopy. *PLoS ONE* **10**, e0145871 (2015).
15. Taherzadeh, D., Picioreanu, C. & Horn, H. Mass Transfer Enhancement in Moving Biofilm Structures. *Biophysical Journal* **102**, 1483–1492 (2012).
16. Von Canstein, H., Ogawa, J., Shimizu, S. & Lloyd, J. R. Secretion of Flavins by *Shewanella* Species and Their Role in Extracellular Electron Transfer. *Appl Environ Microbiol* **74**, 615–623 (2008).
17. Tan, S. L. J., Kan, J. M. & Webster, R. D. Differences in Proton-Coupled Electron-Transfer Reactions of Flavin Mononucleotide (FMN) and Flavin Adenine Dinucleotide (FAD) between Buffered and Unbuffered Aqueous Solutions. *J. Phys. Chem. B* **117**, 13755–13766 (2013).
18. Coursolle, D., Baron, D. B., Bond, D. R. & Gralnick, J. A. The Mtr Respiratory Pathway Is Essential for Reducing Flavins and Electrodes in *Shewanella oneidensis*. *J Bacteriol* **192**, 467–474 (2010).

19. Brutinel, E. D. & Gralnick, J. A. Shuttling happens: soluble flavin mediators of extracellular electron transfer in Shewanella. *Appl Microbiol Biotechnol* **93**, 41–48 (2012).
20. Korth, B., Rosa, L. F. M., Harnisch, F. & Picioreanu, C. A framework for modeling electroactive microbial biofilms performing direct electron transfer. *Bioelectrochemistry* **106**, 194–206 (2015).
21. Torres, C. I. *et al.* A kinetic perspective on extracellular electron transfer by anode-respiring bacteria. *FEMS Microbiol Rev* **34**, 3–17 (2010).
22. Kato Marcus, A., Torres, C. I. & Rittmann, B. E. Conduction-based modeling of the biofilm anode of a microbial fuel cell. *Biotechnol. Bioeng.* **98**, 1171–1182 (2007).
23. Ross, D. E., Brantley, S. L. & Tien, M. Kinetic Characterization of OmcA and MtrC, Terminal Reductases Involved in Respiratory Electron Transfer for Dissimilatory Iron Reduction in *Shewanella oneidensis* MR-1. *Appl Environ Microbiol* **75**, 5218–5226 (2009).
24. Okamoto, A. *et al.* Uptake of self-secreted flavins as bound cofactors for extracellular electron transfer in *Geobacter* species. *Energy Environ. Sci.* **7**, 1357–1361 (2014).
25. Kotloski, N. J. & Gralnick, J. A. Flavin Electron Shuttles Dominate Extracellular Electron Transfer by Shewanella oneidensis. *mBio* **4**, e00553-12 (2013).
26. Okamoto, A., Hashimoto, K., Nealson, K. H. & Nakamura, R. Rate enhancement of bacterial extracellular electron transport involves bound flavin semiquinones. *Proc. Natl. Acad. Sci. U.S.A.* **110**, 7856–7861 (2013).
27. Kato Marcus, A., Torres, C. I. & Rittmann, B. E. Conduction-based modeling of the biofilm anode of a microbial fuel cell. *Biotechnol. Bioeng.* **98**, 1171–1182 (2007).
28. Renslow, R. *et al.* Modeling biofilms with dual extracellular electron transfer mechanisms. *Phys. Chem. Chem. Phys.* **15**, 19262 (2013).
29. Thiele, E. W. Relation between Catalytic Activity and Size of Particle. *Ind. Eng. Chem.* **31**, 916–920 (1939).

30. Aris, R. *Mathematical Theory of Diffusion and Reaction in Permeable Catalysts*. (Oxford University Press, Place of publication not identified, 1975).
31. Torres, C. I., Kato Marcus, A. & Rittmann, B. E. Proton transport inside the biofilm limits electrical current generation by anode-respiring bacteria. *Biotech & Bioengineering* **100**, 872–881 (2008).
32. Kato Marcus, A., Torres, C. I. & Rittmann, B. E. Conduction-based modeling of the biofilm anode of a microbial fuel cell. *Biotechnol. Bioeng.* **98**, 1171–1182 (2007).
33. Stern, O. ZUR THEORIE DER ELEKTROLYTISCHEN DOPPELSCHICHT. *Zeitschrift für Elektrochemie und angewandte physikalische Chemie* **30**, 508–516 (1924).
34. Amadu, M. & Miadonye, A. Interrelationship of Electric Double Layer Theory and Microfluidic Microbial Fuel Cells: A Review of Theoretical Foundations and Implications for Performance. *Energies* **17**, 1472 (2024).
35. Li, C., Hu, S., Ji, C., Yi, K. & Yang, W. Insight into the Pseudocapacitive Behavior of Electroactive Biofilms in Response to Dynamic-Controlled Electron Transfer and Metabolism Kinetics for Current Generation in Water Treatment. *Environ. Sci. Technol.* **57**, 19891–19901 (2023).
36. Wang, H. *et al.* Electrochemical impedance spectroscopy applied to microbial fuel cells: A review. *Front. Microbiol.* **13**, 973501 (2022).
37. Picioreanu, C., Head, I. M., Katuri, K. P., Van Loosdrecht, M. C. M. & Scott, K. A computational model for biofilm-based microbial fuel cells. *Water Research* **41**, 2921–2940 (2007).
38. *The Merck Index: An Encyclopedia of Chemicals, Drugs, and Biologicals*. (The Royal Society of Chemistry, Cambridge, 2013).
39. Tang, Y. J., Meadows, A. L. & Keasling, J. D. A kinetic model describing *Shewanella oneidensis* MR-1 growth, substrate consumption, and product secretion. *Biotech & Bioengineering* **96**, 125–133 (2007).

40. Pinchuk, G. E. *et al.* Constraint-Based Model of Shewanella oneidensis MR-1 Metabolism: A Tool for Data Analysis and Hypothesis Generation. *PLoS Comput Biol* **6**, e1000822 (2010).
41. Bard, A. J., Shea, T. V., Crayston, J. A., Kittlesen, G. P. & Wrighton, M. S. Digital Simulation of the Measured Electrochemical Response of Reversible Redox Couples at Microelectrode Arrays: Consequences Arising from Closely Spaced Ultramicroelectrodes. *Analytical Chemistry* **58**, 2321–2331 (1986).
42. Niwa, O., Morita, M. & Tabei, H. Electrochemical Behavior of Reversible Redox Species at Interdigitated Array Electrodes with Different Geometries: Consideration of Redox Cycling and Collection Efficiency. *Analytical Chemistry* **62**, 447–452 (1990).
43. Dotan, T., Nazarenko, M., Atiya, Y. & Shacham-Diamand, Y. Transport effects in biochip sensors with redox cycling amplification. *Electrochimica Acta* **459**, 142520 (2023).
44. Abboud, R. *et al.* Low-Temperature Growth of *Shewanella oneidensis* MR-1. *Appl Environ Microbiol* **71**, 811–816 (2005).
45. Gao, H., Yang, Z. K., Wu, L., Thompson, D. K. & Zhou, J. Global Transcriptome Analysis of the Cold Shock Response of *Shewanellaoneidensis* MR-1 and Mutational Analysis of Its ClassicalCold ShockProteins. *J Bacteriol* **188**, 4560–4569 (2006).
46. Corts, A. D., Thomason, L. C., Gill, R. T. & Gralnick, J. A. A new recombineering system for precise genome-editing in Shewanella oneidensis strain MR-1 using single-stranded oligonucleotides. *Sci Rep* **9**, 39 (2019).
47. Kouzuma, A., Meng, X.-Y., Kimura, N., Hashimoto, K. & Watanabe, K. Disruption of the Putative Cell Surface Polysaccharide Biosynthesis Gene SO3177 in *Shewanella oneidensis* MR-1 Enhances Adhesion to Electrodes and Current Generation in Microbial Fuel Cells. *Appl Environ Microbiol* **76**, 4151–4157 (2010).

48. Trudicova, M. *et al.* Multiscale Experimental Evaluation of Agarose-Based Semi-Interpenetrating Polymer Network Hydrogels as Materials with Tunable Rheological and Transport Performance. *Polymers* **12**, 2561 (2020).
49. Qu, X. *et al.* Tissue-Adaptable Hydrogel for Mechanically Compliant Bioelectronic Interfaces. *Nano Lett.* **25**, 4759–4766 (2025).
50. Someya, T., Bao, Z. & Malliaras, G. G. The rise of plastic bioelectronics. *Nature* **540**, 379–385 (2016).
51. Ogston, A. G., Preston, B. N. & Wells, J. D. On the transport of compact particles through solutions of chain-polymers. *Proceedings of the Royal Society of London. A. Mathematical and Physical Sciences* **333**, 297–316 (1973).
52. Pluen, A., Netti, P. A., Jain, R. K. & Berk, D. A. Diffusion of Macromolecules in Agarose Gels: Comparison of Linear and Globular Configurations. *Biophysical Journal* **77**, 542–552 (1999).
53. El-Naggar, M. Y. *et al.* Electrical transport along bacterial nanowires from *Shewanella oneidensis* MR-1. *Proc. Natl. Acad. Sci. U.S.A.* **107**, 18127–18131 (2010).
54. Gorby, Y. A. *et al.* Electrically conductive bacterial nanowires produced by *Shewanella oneidensis* strain MR-1 and other microorganisms. *Proc. Natl. Acad. Sci. U.S.A.* **103**, 11358–11363 (2006).
55. Kotloski, N. J. & Gralnick, J. A. Flavin Electron Shuttles Dominate Extracellular Electron Transfer by Shewanella oneidensis. *mBio* **4**, e00553-12 (2013).
56. Marsili, E. *et al. Shewanella* secretes flavins that mediate extracellular electron transfer. *Proc. Natl. Acad. Sci. U.S.A.* **105**, 3968–3973 (2008).
57. Logan, B. E. *et al.* Microbial Fuel Cells: Methodology and Technology. *Environ. Sci. Technol.* **40**, 5181–5192 (2006).
58. Torres, C. I. *et al.* A kinetic perspective on extracellular electron transfer by anode-respiring bacteria. *FEMS Microbiol Rev* **34**, 3–17 (2010).

59. Trudicova, M. *et al.* Multiscale Experimental Evaluation of Agarose-Based Semi-Interpenetrating Polymer Network Hydrogels as Materials with Tunable Rheological and Transport Performance. *Polymers* **12**, 2561 (2020).
60. Riedel, R., Rani, G. & Sengupta, A. Bacterial Adhesion on Soft Surfaces: The Dual Role of Substrate Stiffness and Bacterial Growth Stage. *Microorganisms* **13**, 637 (2025).
61. Pu, X., Wu, Y., Liu, J. & Wu, B. 3D Bioprinting of Microbial-based Living Materials for Advanced Energy and Environmental Applications. *Chem Bio Eng.* **1**, 568–592 (2024).
62. Budharaju, H., Sundaramurthi, D. & Sethuraman, S. Embedded 3D bioprinting – An emerging strategy to fabricate biomimetic & large vascularized tissue constructs. *Bioactive Materials* **32**, 356–384 (2024).
63. Pernodet, N., Maaloum, M. & Tinland, B. Pore size of agarose gels by atomic force microscopy. *Electrophoresis* **18**, 55–58 (1997).
64. Amsden, B. Solute Diffusion within Hydrogels. Mechanisms and Models. *Macromolecules* **31**, 8382–8395 (1998).

Acknowledgements

Author Contribution Statement

T.D. contributed by Conceptualization, Investigation, Writing – original draft, Methodology, Visualization, Formal analysis; L.H.N., C.O., and E.R.M contributed by Investigation; A.L.F contributed by Conceptualization, Writing - review & editing, Funding acquisition, Project administration, Supervision, Resources.

Ethics declarations

Competing interests

There are no conflicts of interest to declare.